

Deformation of an Al-7Mg alloy with extensive structural micro-segregations during dynamic plastic deformation

Shenbao Jin¹, Nairong Tao², Knut Marthinsen¹ and Yanjun Li^{1,*}

1. Department of Materials Science and Engineering, Norwegian University of Science and Technology,

7491 Trondheim, Norway

2. Shenyang National Laboratory for Materials Science, Institute of Metal Research, Chinese Academy

of Sciences, Shenyang, 110016, China

*** Corresponding author at: Department of Materials Science and Engineering,**

Norwegian University of Science and Technology, 7491 Trondheim, Norway

E-mail address: Yanjun.Li@ntnu.no (Y.J. Li).

Abstract

The microstructure evolution and deformation behavior of an as-cast Al-7Mg alloy with severe Mg segregation zones distributed on grain boundaries and in interdendrite regions subjected to dynamic plastic deformation (DPD) at both room and liquid nitrogen temperatures have been studied. At low strains, the deformation of the material is found to be mainly through the formation of deformation bands. At high strains, globular ultrafine grains form in the materials due to continuous dynamic recrystallization, which is also the dominant grain refinement mechanism. After deformation to strain of 1.0, the Mg segregation zones are deformed into fine parallel bands distributing along the deformation bands. Moreover, it is revealed that Al_8Mg_5 particles and the Mg segregation can enhance the formation of deformation bands even in grains with a stable orientation, namely those with one of the $\{101\}$ planes perpendicular to the compression direction, which can reduce the inhomogeneity of the deformation structure.

1. Introduction

Al-Mg alloys are of interest in automobile and aerospace industries due to their light weight, high specific strength and high resistance to corrosion. In the last decades, different severe plastic deformation (SPD) techniques such as equal channel angular pressing (ECAP) [1-9] and high pressure torsion (HPT) [10-12] that can efficiently produce ultra-fine-grained and nanostructured materials have been extensively applied to Al-Mg alloys with the aim to further increase the strength of the alloys. In contrast to the SPD techniques, dynamic plastic deformation (DPD) with high strain rate (10^2 - 10^3 s⁻¹) has been developed for the materials with low and medium stacking fault energies (SFEs) [13-16] and the materials with the hexagonal crystal structure [17-20], with the aim of producing nano-crystalline and nano-twin microstructures. However, for materials with high SFEs, for example, pure Al, deformation twinning has never been observed during DPD [21]. According to the calculations in [22], the SFEs of the Al-Mg alloys decrease with increasing Mg content. Moreover, among all the Al alloys, Al-Mg alloys are supposed to have the largest tendency to form deformation twinning [23]. Therefore, it is of interest to investigate the deformation behavior of high Mg-content Al-Mg alloys during DPD.

However, as pointed out in [8] and [24], Al-Mg alloys with a high Mg content are difficult to be severely deformed because cracks are prone to occur. In fact, since the equilibrium solid solubility of Mg in Al is only about 1 wt.% at room temperature [25], Mg can hardly be uniformly distributed in the Al matrix in the as-cast state. At high cooling rate, the Al₈Mg₅ compound, usually denoted as Al₃Mg₂, precipitates along grain boundaries and in the interdendritic regions even in Al-Mg alloys with 2-3 wt.% Mg [26]; while during deformation, Mg tends to distribute along deformation-distorted grain boundaries [24,27,28]. The precipitation of Al₈Mg₅ and the segregation of Mg to grain boundaries have significant influence on the performance of the Al-Mg alloys. It has been reported that intergranular fracture is more

likely to happen during fatigue and creep testing when Mg segregates at grain boundaries [29,30]. An explanation was given in [31] based on first-principle-calculations result that Mg segregation decreases the cohesive strength of the boundary. However, a contrary effect of Mg segregation on boundary strength was reported in [32]. On the other hand, high Mg content solution could induce an increase in the microstructural inhomogeneity of Al-Mg alloys after SPD. For example, it was reported that more passes are necessary to establish a homogeneous microstructure with increasing Mg content in Al alloy during ECAP [4]. For a high Mg content binary Al-7Mg alloy, a highly inhomogeneous microstructure, i.e., bimodal structure consisting of both coarse micron-sized crystallites and ultrafine grains with mean sizes of $< \sim 500$ nm is usually developed [8,9,33]. Then, whether this microstructure inhomogeneity of Al-Mg alloy can be suppressed by the Mg segregation that exists in the initial microstructure becomes an important question. Besides, in spite of these aforementioned works, an in-depth analysis of the effect of Mg segregation and Al_3Mg_5 particles on deformation of high-Mg content Al-Mg alloys during high strain rate deformation is still mainly missing.

Therefore, in this paper, an as-cast Al-7Mg alloy with extensive structural micro-segregations was subjected to DPD at room temperature (RT) and liquid nitrogen temperature (LNT). The evolution of the deformation structure and the influence of the Mg segregation on the deformation zones have been investigated in detail by scanning electron microscopy following deformation at liquid nitrogen temperature and at room temperature to different strains. The corresponding evolution in hardness has been monitored by micro-hardness measurements.

2. Experimental

The material used in this study was a DC-cast Al-7Mg alloy ingot with dimension of $\text{Ø}96 \times 1200$ mm, which was supplied by Hydro Aluminum and with the chemical composition (in wt.%) of 7.0Mg, 0.05Fe,

0.06Si and Al (balance). Cylindrical samples (10 mm in diameter and 15 mm in thickness) were machined for DPD processing. The cylindrical samples were then compressed by an upper anvil at RT and LNT with a high loading rate ($\sim 100\text{-}1000\text{ s}^{-1}$). The impacting energy during each impact was 800 J. In order to maintain high strain rate, the deformation was achieved by multiple impacts with a thickness reduction of 2 mm in each impact. The deformation strain is defined as $\varepsilon = \ln(L_0/L_f)$, where L_0 and L_f are initial and final thickness of the deformed sample, respectively. The samples were deformed to strains of $\varepsilon = 0.45$ and 0.97 at RT, and $\varepsilon = 0.25$ and 0.43 at LNT.

Backscattered electron (BSE), scanning electron microscopy (SEM) and energy dispersive X-ray spectrometry (EDS) analyses of particles and Mg segregation were performed on the longitudinal section, namely, the transverse direction (TD)-compression direction (CD) plane, as indicated in Fig. 1(a), with accelerating voltages of 15 and 20 kV, respectively. The deformation structure was characterized by electron backscattered diffraction (EBSD) which was conducted in a Zeiss 55 VP field emission gun SEM (FEG-SEM) equipped with a Nordif EBSD detector and TSL OIM software. An acceleration voltage of 20 kV, a working distance of 20 mm, and scan steps of $0.05\text{-}0.1\ \mu\text{m}$ were employed. The grain sizes along longitudinal and cross directions were measured from the EBSD images using the line intercept method. Here, it should be pointed out that the orientations of the EBSD maps in the present paper are all correspond to the RD (radial direction)-TD plane since a 90° rotation around TD axis was made on initial orientations, which is helpful to understand the relationship between the orientation changes within the grains under the compression strain. Micro-hardness measurements were carried out on the TD-RD plane using a DKV-1S Vickers hardness testing machine with a load of 500 g and a loading time of 10 s. The hardness values obtained were averaged from at least ten separate measurements.

3. Results

3.1. Solidification structure of Al-7Mg

As shown in Fig. 1(b), the as-cast microstructure of the Al-7Mg alloy consists of α -Al grains with an average size of 75 μm , a large fraction of Al_8Mg_5 particles and a small fraction of fine block-shaped Al_6Fe and Mg_2Si particles. The formation of Al_8Mg_5 particles is due to the segregation of Mg during solidification which is a result of the enrichment of Mg in the liquid at the later stages of solidification. When the Mg content reaches a eutectic composition of 35 wt.% Mg, an eutectic reaction, $\text{L} \rightarrow \alpha\text{-Al} + \text{Al}_8\text{Mg}_5$, takes place at 450 °C. Most of the Al_8Mg_5 particles have a chain-like morphology and are located in the interdendritic regions and at grain boundaries. A high concentration of Mg can clearly be seen at these locations from the EDS element mapping of Mg (Fig. 2c). Moreover, from the EDS line profiles of the Mg concentration along and cross dendrite arms of Grain1 (L1 and L2, Figs. 2a and b), it can be seen that the Mg concentration is the lowest (~3 wt.%) at the center area of the grain, while it increases towards the tip of dendrite arms or grain boundaries. At some grain boundaries, the Mg concentration is as high as 33.8 wt.% (Fig. 2b), which should be attributed to the large Al_8Mg_5 intermetallic precipitates. In the interdendritic areas without Al_8Mg_5 particles, the Mg concentration, i.e., 6-8.5 wt.% as shown in Fig. 2(c), is still much higher than the nominal concentration of the alloys. It is interesting to note that tiny misorientations (smaller than 2°) exist between different dendrite arms, as can be seen from Fig. 2(d).

3.2. Deformation structure after DPD at RT

Fig. 3 shows the microstructure of the Al-7Mg alloy as deformed to a strain of 0.45 by DPD at RT. As shown in Figs. 3(a) and (b), only a small fraction of the Al_8Mg_5 particles were broken up and slightly refined while the original morphology of the dendrite arms and the segregation zones within interdendritic regions can still be seen. In the EBSD map (Fig. 3c) of the same area as in Figs. 3(a) and (b), it can be seen

that many deformation bands have formed in the interior of original as-cast grains while cell structures or sub-grain structures can be seldom observed. This is different from pure aluminum subjected to DPD [21] or Al-7Mg alloy subjected to ECAP [8,9,33] where greatly refined sub-grains/cell structures formed in both of these two processes. This should be attributed to the special deformation behavior of the Al-7Mg alloy during DPD. It is known that the deformation of Al-Mg alloys with a high Mg content is mainly through the planar glide mode [34,35]; and the tendency for planar glide increases with increasing Mg solid solution content or strain rate, or decreasing deformation temperature. During DPD, the high strain rate and mono-directional deformation will further strengthen the planar glide deformation mode.

Here, it is worth mentioning that there are much less deformation bands and low-angle grain boundaries (LAGBs) in grains indexed with a green color, like the grain labeled as Grain2 in Fig. 3(c), than those grains with purple or red colors. It implies those dark green grains have a more stable orientation and it is difficult for deformation bands to form in these grains. However, some LAGBs can still be observed in these grains, for instance in Grain2, and interestingly these LAGB are coincident with the boundary between the Mg segregation zone and the original dendrite arms of the Al grain. It indicates that the Mg segregation zones in the interdendritic areas have enhanced the formation of deformation bands. This is due to the high strength of the Mg-enriched zone in comparison to the surrounding matrix, which causes the incompatibility in deformation between the Mg segregation zones and the surrounding matrix. As shown in Figs. 3(c) and (d), the misorientation angles of the boundaries of the deformation bands connected with the Al_8Mg_5 particles are relatively higher (along L5) than those located on the zones with a lower Mg concentration (along L6).

After further deformation to a strain of 0.97, the large Al_8Mg_5 particles are subdivided into smaller particles and randomly distributed along the elongated grain boundaries (Fig. 4a). Moreover, it can be seen

from Fig. 4 (b) that most of the Mg solute aggregates along the elongated grain boundaries. These elongated grain boundaries are always with high misorientation angles; while in some larger elongated grains, sub-grains enclosed by low- and moderate-angle boundaries are developed (Fig. 4c). According to Figs. 4(d)-(g), the segregation level of Mg varies strongly at the grain boundaries with different misorientation angles. Obviously, relatively higher Mg concentrations can be found at boundaries with higher misorientation angles, while lower Mg concentrations are observed on the low- and moderate-angle boundaries. This result indicates that the high angle grain boundaries are more preferential to form along Mg segregation zones.

With increasing strain from 0.45 to 0.97, the purple or red grains are highly deformed and become quite elongated because of the extensively formed inter-grain deformation bands and the extension of the deformation bands under the compressive strain; while the coarse green grains are also subdivided into many substructures by more developed deformation bands, as can be seen from Fig. 5(a). Then, the microstructural refinement process will proceed through dynamic recrystallization. As indicated in Fig. 5(a), the substructures having very low misorientations are developed in the grains and deformation bands. From grain interior to the grain boundary, the misorientation increases gradually, as shown in Figs. 5(b) and (c). A similar phenomenon was found in Al-5Mg alloy deformed in plane strain compression at 350 °C [36]. It was speculated that the gradient of misorientation from grain center to edge is induced by the progressive rotation of subgrains/substructures adjacent to pre-existing grain boundaries when the material is strained; and through this rotation, new grains enclosed by high-angle boundaries finally form at the original grain boundaries at higher strains, for example, the grains pointed by black arrow in Fig. 5(a). This rotation recrystallization should be associated with the distinct lattice rotation speeds between the center zone of a grain and the zone close to grain boundaries as well as the accelerated dynamic recovery in the

grain boundary regions [36]. Actually, this rotation dynamic recrystallization was usually reported for the Al-Mg alloys deformed at elevated temperatures [37,38] because high temperature facilitates the lattice rotation. However, in our experiment, the Mg segregation and Al_8Mg_5 particles on the grain boundaries seriously retard the grain boundary mobility, and can also induce high density of dislocations in the vicinity of the grain boundaries during deformation, which will provide relatively higher driving force for dynamic recovery. Therefore, this mechanism of rotation dynamic recrystallization, which can be considered as one type of continuous dynamic recrystallization (CDRX), occurs in the Al-7Mg alloy deformed by DPD at higher strains.

3.3. Microstructure of the Al-7Mg samples deformed at LNT

Fig. 6 shows typical orientation images of the DPD samples deformed at LNT. As deformed to a low strain of $\varepsilon = 0.25$, similar to the deformation structure as deformed to $\varepsilon = 0.45$ at RT, many of the coarse grains have been subdivided into deformation bands. These inter-grain deformation bands enclosed by low angle boundaries form and therefore subdivide the original coarse grains into different orientation regions (Fig. 6a). These substructures slip independently when subjected to further deformation, inducing an increase in the misorientation angles of the surrounding boundaries and finally formation of the finer grains enclosed with high-angle boundaries (Fig. 6b).

It is worth noting that the deformation bands initiated by the Al_8Mg_5 particles can also be found in the green grains in the DPD samples deformed at LNT. Moreover, compared to the Al-7Mg alloy deformed at RT, more deformation bands are developed in the Al-7Mg alloy at the cryogenic temperature. That is because low deformation temperature is beneficial for formation of the deformation bands. In other words, the microstructure is refined more efficiently at LNT. Nevertheless, the stress concentration caused by Al_8Mg_5 particles and Mg segregations on the grain boundaries limits the maximal strains of the DPD

samples, i.e., $\varepsilon_{max} = 0.97$ and 0.43 at RT and LNT, respectively. Therefore, the CDRX is suppressed at the cryogenic temperature because of the limited strain and the grains have not been greatly refined.

As mentioned previously, the misorientation angles of the deformation bands will increase gradually during deformation, which can be seen from Fig. 7(a). As indicated, high densities of low angle boundaries form at $\varepsilon = 0.43$ at RT and 0.25 at LNT; while some of them evolve into boundaries with higher misorientation angles ($5\text{-}20^\circ$) at $\varepsilon = 0.97$ at RT and 0.42 at LNT. Since the samples cannot be further deformed, a further increase in the misorientation angles of the boundaries between deformation bands and grain boundaries is restrained. It is known that the dislocation density during deformation is controlled by the competition between the dislocation generation rate and the annihilation rate. Because the latter is suppressed by both the high strain rate and low deformation temperature, the samples deformed at LNT will have higher density of dislocations than those deformed at RT. Fig. 7(b) shows the grain sizes in the RT-DPD and LNT-DPD Al-7Mg samples. As indicated, the grains are refined from about 85 to $10\ \mu\text{m}$ after DPD. According to the Hall-Petch relationship, the hardness increase caused by such a grain refinement can be ignored. Therefore, the high density of dislocations formed during deformation should be the primary source of the hardness increase, which also explains why the LNT-DPD samples have higher hardness with even lower deformation strains (Fig. 7c).

4. Discussion

It is known that the formation of the deformation bands in polycrystalline materials is mainly controlled by the grain orientations. As can be seen from Fig. 3(c) and Fig. 6, there are mainly two types of grains in the DPD samples: large green grains with less deformation bands and grains indexed with red and violet colors that are greatly subdivided by deformation bands. As we have mentioned, the orientation given in the EBSD images are all in the TD-RD plane, i.e., which is perpendicular to the CD. Hence, the

large green grains have one of their $\{101\}$ planes perpendicular to the CD; while for the red and violet grains, their $\langle 101 \rangle$ directions are far away from the CD.

For these green grains, four slip systems $(111)[01\bar{1}]$, $(111)[1\bar{1}0]$, $(\bar{1}\bar{1}1)[011]$ and $(\bar{1}\bar{1}1)[110]$ with an equivalent Schmid factor of 0.408 will be simultaneously activated. This multiple slip orientation is stable against lattice rotations and will induce a homogeneous dislocation distribution in the grain [39]. In other words, the green grains are oriented favorably to accommodate the compression strains and thus can undergo large deformation without much subdivision and are deformed into elongated shape. However, in the present work, deformation bands can also be found in the green grains, and the locations of these inter-grain deformation bands are always coincident with the Mg segregation zones. This is because the local parts with a highly segregated Mg content in the grains can hardly collaboratively deform with the surrounding part of Al grain. These results indicate that the Mg segregation can enhance the formation of deformation bands even in those grains with a stable orientation. It can be seen from Fig. 3(c) and Fig. 6 that the parallel deformation bands in different local areas of coarse grains can have different orientations. That should be attributed to different slips of the deformation bands on different $\{111\}$ slip planes. In contrast, the deformation bands aligned with the Mg segregation zones are not parallel to each other, because the Mg segregation zones are located at the interdendritic regions and grain boundaries. Anyway, the above results indicate that the green grains can also be refined by formation of deformation bands because of the severe Mg segregation, which reduces the microstructure inhomogeneity in Al-7Mg alloys during DPD, or in other words, improves the efficiency of the grain refinement.

On the other hand, for the red and violet grains with their $\langle 101 \rangle$ far away from the CD, numerous inter-grain deformation bands have to be developed to help accommodating the compression strains because of the lack of the cross slip, and thus these grains are gradually subdivided during DPD into small

sub-grains by deformation bands. Actually, in Al-Mg alloy with high Mg concentration, the grains with orientation $\langle 101 \rangle$ far away from the CD will become more difficult to accommodate the compression strain because solute Mg atoms reduce the dislocation mobility. Moreover, the dislocation movement can be further suppressed by the high strain rate during DPD and also at cryogenic temperatures. Therefore, these grains will be highly subdivided and refined by formation of numerous deformation bands. At high strains, CDRX works in the deformation bands for formation of equiaxed or small elongated grains with row stacking configuration, as shown in Fig. 4(c).

5. Conclusions

In summary, during DPD of a high Mg-content aluminium alloy, i.e. Al-7Mg, severe Mg segregation in the as-cast microstructure is refined and mainly distributed along the elongated grain boundaries. Moreover, the Mg segregation and/or Al_8Mg_5 particles can be the sources for formation of the inter-grain deformation bands, especially in the grains with their $\langle 101 \rangle$ orientation close to the CD. Thus, Al_8Mg_5 particles and Mg segregation can significantly reduce the microstructure inhomogeneity in Al-7Mg alloys during deformation and improve the efficiency of the grain refinement.

Acknowledgements

Financial support from Research Council of Norway, under the FRINATEK project ‘BENTMAT’ (Project number 222173) is gratefully acknowledged.

References

- [1] J.T. Wang, Z.J. Horita, M. Furukawa, M. Nemoto, N.K. Tsenev, R.Z. Valiev, Y. Ma, T.G. Langdon, J. Mater. Res. 8 (1993) 2810–2818.
- [2] J. Wang, Y. Iwahashi, Z. Horita, M. Furukawa, M. Nemoto, R.Z. Valiev, Acta Mater. 44 (1996) 2973–2982.

- [3] M. Furukawa, Z. Horita, M. Nemoto, R.Z. Valiev, T.G. Langdon, *Acta Mater.* 44 (1996) 4619–4629.
- [4] Y. Iwahashi, Z. Horita, M. Nemoto, T.G. Langdon, *Metall. Mater. Trans. A* 29 (1998) 2503–2510.
- [5] D.G. Morrisa, M.A. Muñoz-Morrisa, *Acta Mater.* 50 (2002) 4047–4060.
- [6] Y.J. Chen, H.J. Roven, S.S. Gireesh, P.C. Skaret, J. Hjelen, *Mater. Lett.* 65 (2011) 3472–3475.
- [7] Y.J. Chen, Y.C. Chai, H.J. Roven, S.S. Gireesh, Y.D. Yu, J. Hjelen, *Mater. Sci. Eng. A* 545 (2012) 139–147.
- [8] M. Zha, Y.J. Li, R.H. Mathiesen, R. Bjørge, H.J. Roven, *Mater. Sci. Eng. A* 586 (2013) 374–381.
- [9] M. Zha, Y.J. Li, R.H. Mathiesen, R. Bjørge, H.J. Roven, *Mater. Sci. Eng. A* 598 (2014) 141–146.
- [10] G. Nurislamova, X. Sauvage, M. Murashkin, R. Islamgaliev, R. Valiev, *Phil. Mag. Lett.* 88 (2008) 459–466.
- [11] M.P. Liu, H.J. Roven, M. Murashkin, R.Z. Valiev, *Mater. Sci. Eng. A* 503 (2009) 122–125.
- [12] M.P. Liu, H.J. Roven, X.T. Liu, M. Murashkin, R.Z. Valiev, T. Ungár, L. Balogh, *J. Mater. Sci.* 45 (2010) 4659–4664.
- [13] Y.S. Li, N.R. Tao, K. Lu, *Acta Mater.* 56 (2008) 230–241.
- [14] Y. Zhang, N.R. Tao, K. Lu, *Acta Mater.* 59 (2011) 6048–6058.
- [15] F.K. Yan, G.Z. Liu, N.R. Tao, K. Lu, *Acta Mater.* 60 (2012) 1059–1071.
- [16] H.T. Wang, N.R. Tao, K. Lu, *Acta Mater.* 60 (2012) 4027–4040.
- [17] X.Y. Zhang, Y.T. Zhu, Q. Liu, *Scripta Mater.* 63 (2010) 387–390.
- [18] F. Xu, X.Y. Zhang, H.T. Ni, Q. Liu, *Mater. Sci. Eng. A* 541 (2012) 190–195.
- [19] F. Xu, X.Y. Zhang, H.T. Ni, Y.M. Cheng, Y.T. Zhu, Q. Liu, *Mater. Sci. Eng. A* 564 (2013) 22–33.
- [20] C. Lou, X.Y. Zhang, G.L. Duan, J. Tu, Q. Liu, *J. Mater. Sci. Technol.* 30 (2014) 41–46.
- [21] F. Huang, N.R. Tao, *J. Mater. Sci. Technol.* 27 (2011) 1–7.

- [22] T.C. Schulthess, P.E.A. Turchi, A. Gonis, T.G. Nieh, *Acta Mater.* 46 (1998) 2215–2221.
- [23] M. Muzyk, Z. Pakiela, K.J. Kurzydowski, *Scripta Mater.* 64 (2011) 916–918.
- [24] X.Y. Liu, J.B. Adams, *Acta Mater.* 46 (1998) 3467–3476.
- [25] T.B. Massalski, *Binary Alloys Phase Diagrams*, ASM International, Materials Park, OH, 1991.
- [26] N.A. Belov, A.A. Aksenov, *Iron in Aluminum Alloys: Impurity and Alloying Element* Taylor & Francis Inc, New York (2002).
- [27] I.A. Ovid'ko, A.G. Sheinerman, R.Z. Valiev, *J. Mater. Sci.* 49 (2014) 6682–6688.
- [28] X. Sauvage, N. Enikeev, R. Valiev, Y. Nasedkina, M. Murashkin, *Acta Mater.* 72 (2014) 125–136.
- [29] S.H. Na, M.S. Yang, S.W. Nam, *Scripta Metall. Mater.* 32 (1995) 627–632.
- [30] R.G. Song, M.K. Tseng, B.J. Zhang, J. Liu, Z.H. Jin, K.S. Shin, *Acta Mater.* 44 (1996) 3241–3248.
- [31] X.G. Liu, X.W. Wang, J.Y. Wang, H.Y. Zhang, *J. Phys.: Condens. Matter.* 17 (2005) 4301–4308.
- [32] V.I. Razumovskiy, A.V. Ruban, I.M. Razumovskii, A.Y. Lozovoi, V.N. Butrim, Yu.Kh. Vekilov, *Scripta Mater.* 65 (2011) 926–929.
- [33] M. Zha, Y.J. Li, R.H. Mathiesen, R. Bjørge, H.J. Roven, *Acta Mater.* 84 (2015) 42–54.
- [34] D.A. Hughes, *Acta Metall. Mater.* 41 (1993) 1421–1430.
- [35] F.R.N. Nabarro, M.S. Duesbery, *Dislocations in Solids*, vol. 11, Elsevier Science, Amsterdam, 2002.
- [36] F.J. Humphreys, M. Hatherly, *Recrystallization and Related Annealing Phenomena*, Pergamon Press, New York (1995).
- [37] K.J. Gardner, R. Grimes, *Metal Sci.* 13 (1979) 216–222.
- [38] M.D. Drury, F.J. Humphreys, *Acta Metall.* 34 (1986) 2259–2271.
- [39] D. Caillard, J.L. Martin, *Thermally Activated Mechanisms in Crystal Plasticity*, Pergamon (2003).

Figure captions

Figure 1 (a) Ketch map of the DPD sample showing the compression, transverse and radial directions; and (b)-(d) BSE, EDS and EBSD maps for the original as-cast Al-7Mg alloy, respectively. (Black areas on the EBSD image are caused by Al_8Mg_5 particles as they give very poor or totally no index patterns during EBSD scanning)

Figure 2 (a)-(c) EDS line profiles of Mg concentration along L1, L2 and L3 in Fig. 1(c), respectively, and (d) misorientation profile measured along L4 in Fig. 1(d).

Figure 3 (a)-(c) SEM, EDS and EBSD maps for the sample with $\epsilon = 0.45$ at RT, respectively; and (d) and (e) misorientation profiles measured along L5 and L6 in Fig. 3(c), respectively. The unit triangle denotes the crystallographic orientations.

Figure 4 (a)-(c) SEM, EDS and EBSD maps for the sample with $\epsilon = 0.97$ at RT, respectively; (d) and (e) EDS line profiles of Mg concentration along L7 and L8 in Fig. 4(b); and (f) and (g) misorientation profiles measured along L9 and L10 in Fig. 4(c).

Figure 5 (a) Typical EBSD map for the sample with $\epsilon = 0.97$ at RT; and (b) and (c) misorientation profiles measured along L11 and L12 in Fig. 5(a), respectively.

Figure 6 Typical EBSD maps of the TD-RD plane of Al-7Mg samples after deformed to different strains: (a) $\epsilon = 0.25$ and (b) $\epsilon = 0.43$ at LNT.

Figure 7 (a) Misorientation distribution with increasing strain at RT and LNT; and (b) grain sizes and (c) hardness of the DPD samples with different strains.

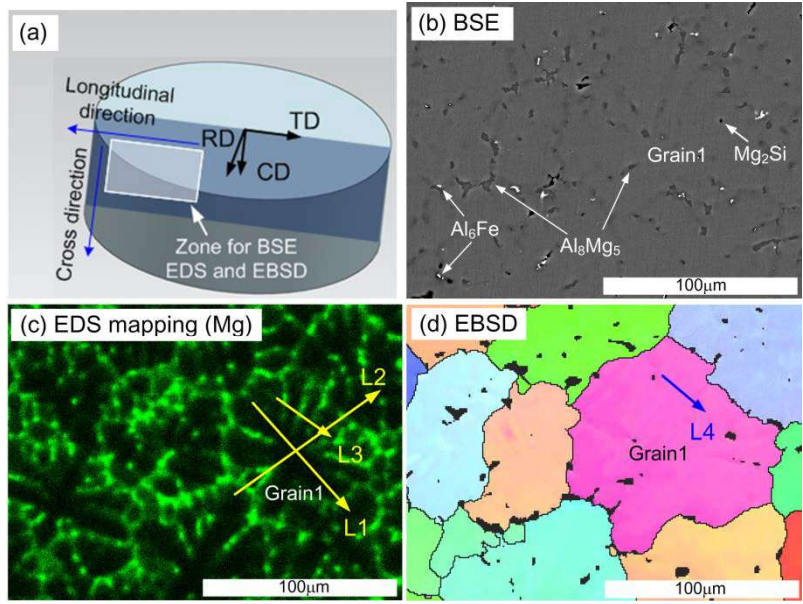


Figure 1 (a) Ketch map of the DPD sample showing the compression, transverse and radial directions; and (b)-(d) BSE, EDS and EBSD maps for the original as-cast Al-7Mg alloy, respectively. (Black areas on the EBSD image are caused by Al_8Mg_5 particles as they give very poor or totally no index patterns during EBSD scanning)

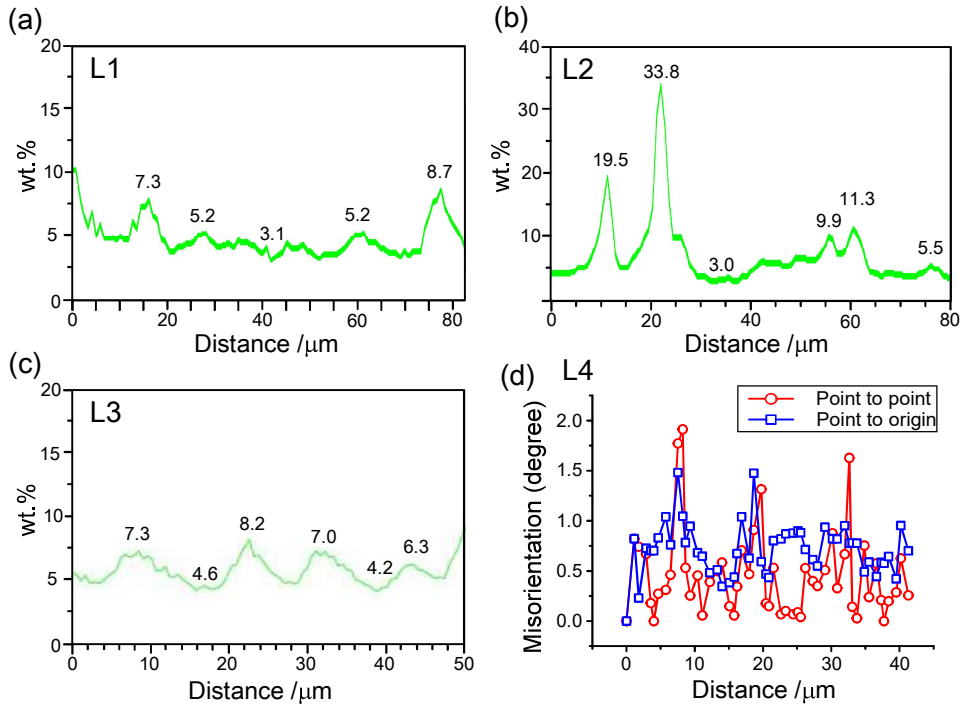


Figure 2 (a)-(c) EDS line profiles of Mg concentration along L1, L2 and L3 in Fig. 1(c), respectively, and (d) misorientation profile measured along L4 in Fig. 1(d).

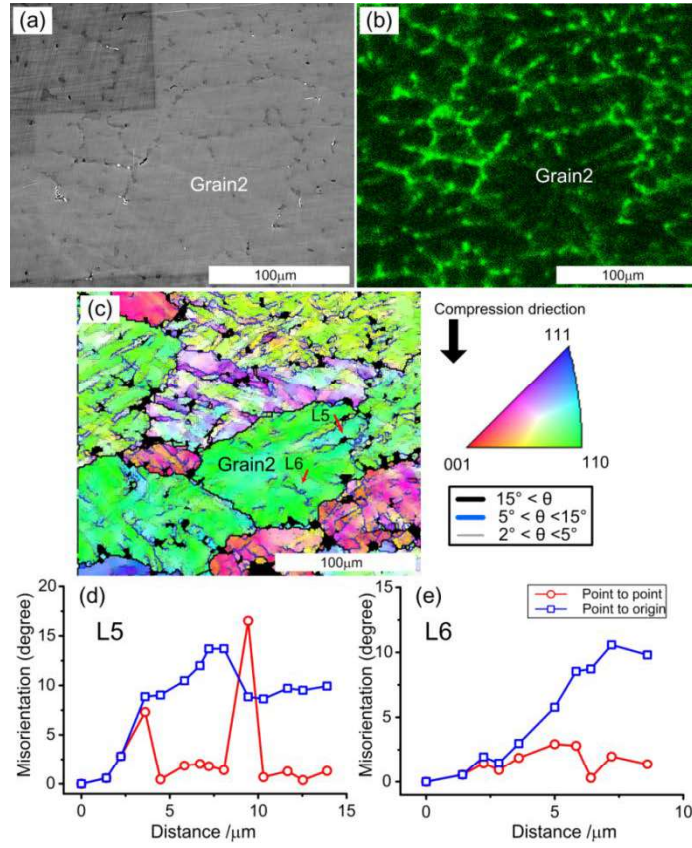


Figure 3 (a)-(c) SEM, EDS and EBSD maps for the sample with $\epsilon = 0.45$ at RT, respectively; and (d) and (e) misorientation profiles measured along L5 and L6 in Fig. 3(c), respectively. The unit triangle denotes the crystallographic orientations.

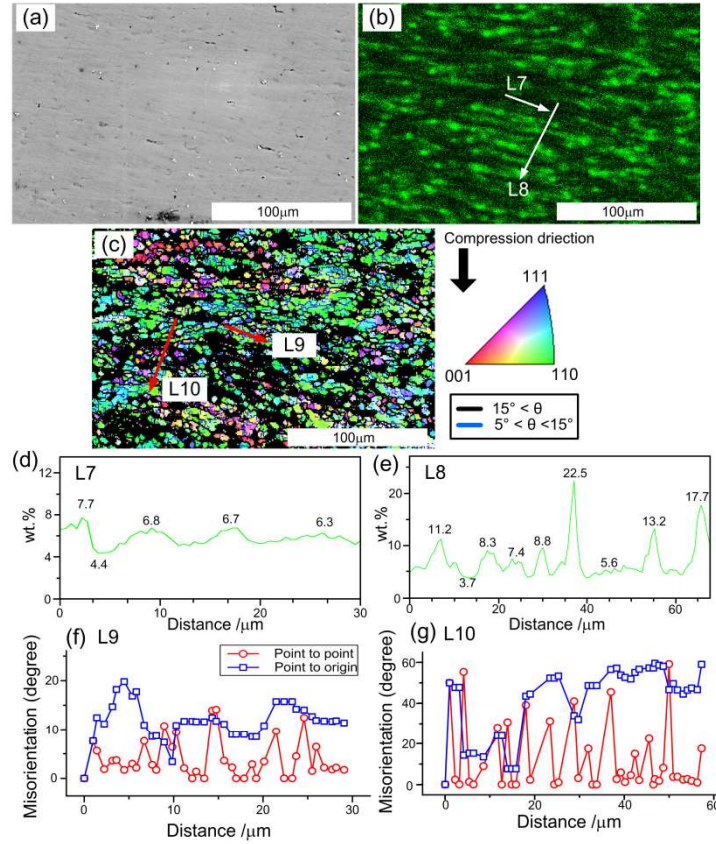


Figure 4 (a)-(c) SEM, EDS and EBSD maps for the sample with $\varepsilon = 0.97$ at RT, respectively; (d) and (e) EDS line profiles of Mg concentration along L7 and L8 in Fig. 4(b); and (f) and (g) misorientation profiles measured along L9 and L10 in Fig. 4(c).

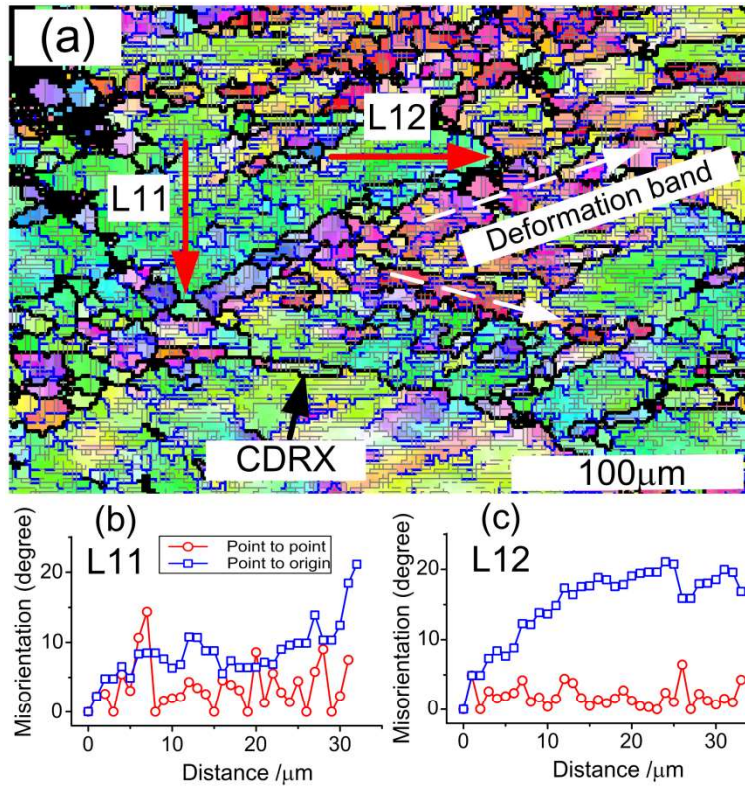


Figure 5 (a) Typical EBSD map for the sample with $\epsilon = 0.97$ at RT; and (b) and (c) misorientation profiles measured along L11 and L12 in Fig. 5(a), respectively.

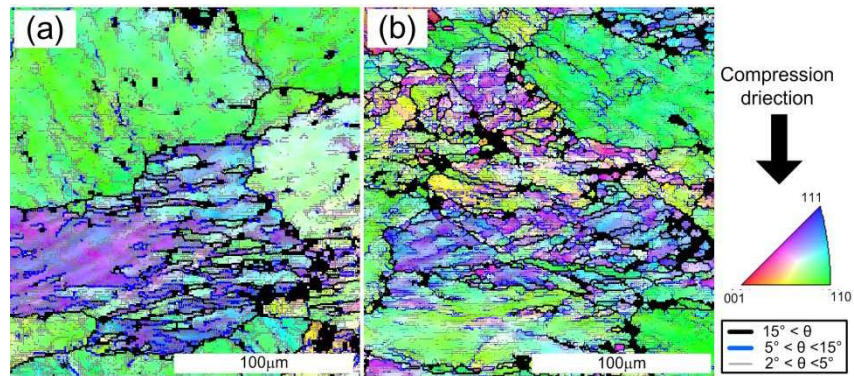


Figure 6 Typical EBSD maps of the TD-RD plane of Al-7Mg samples after deformed to different strains: (a) $\epsilon = 0.25$ and (b) $\epsilon = 0.43$ at LNT.

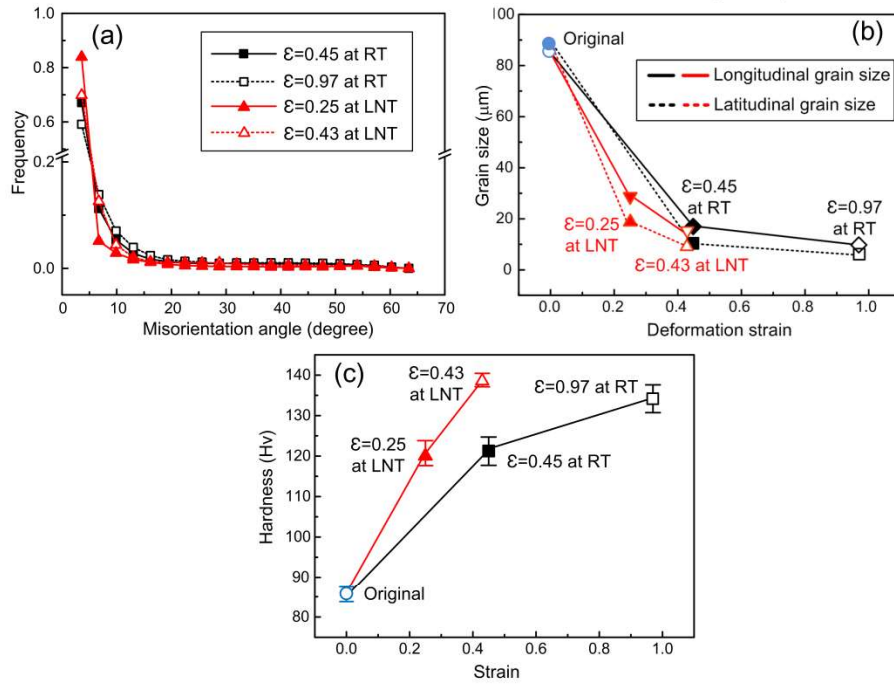


Figure 7 (a) Misorientation distribution with increasing strain at RT and LNT; and (b) grain sizes and (c) hardness of the DPD samples with different strains.

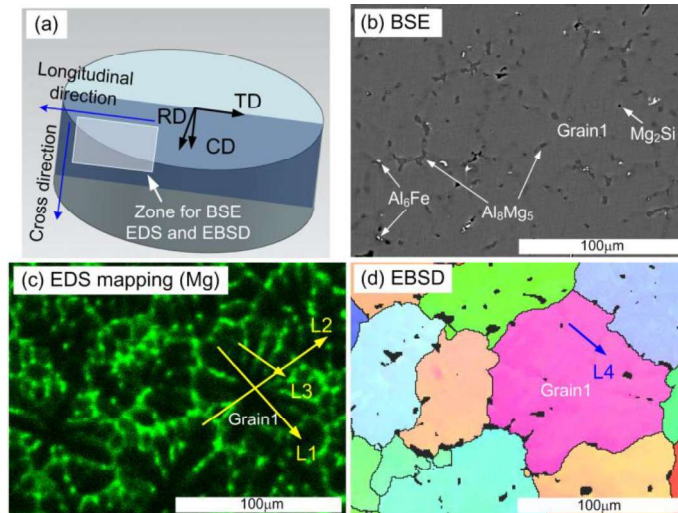


Figure 1 (a) Ketch map of the DPD sample showing the compression, transverse and radial directions; and (b)-(d) BSE, EDS and EBSD maps for the original as-cast Al-7Mg alloy, respectively. (Black areas on the EBSD image are caused by Al₃Mg₅ particles as they give very poor or totally no index patterns during EBSD scanning)

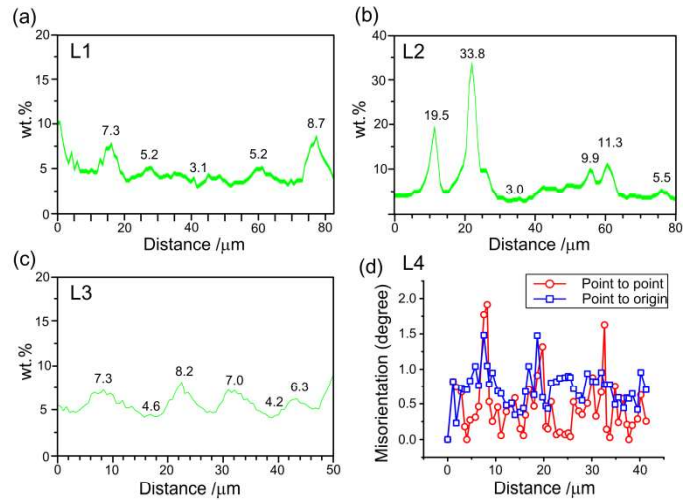


Figure 2 (a)-(c) EDS line profiles of Mg concentration along L1, L2 and L3 in Fig. 1(c), respectively, and

(d) misorientation profile measured along L4 in Fig. 1(d).

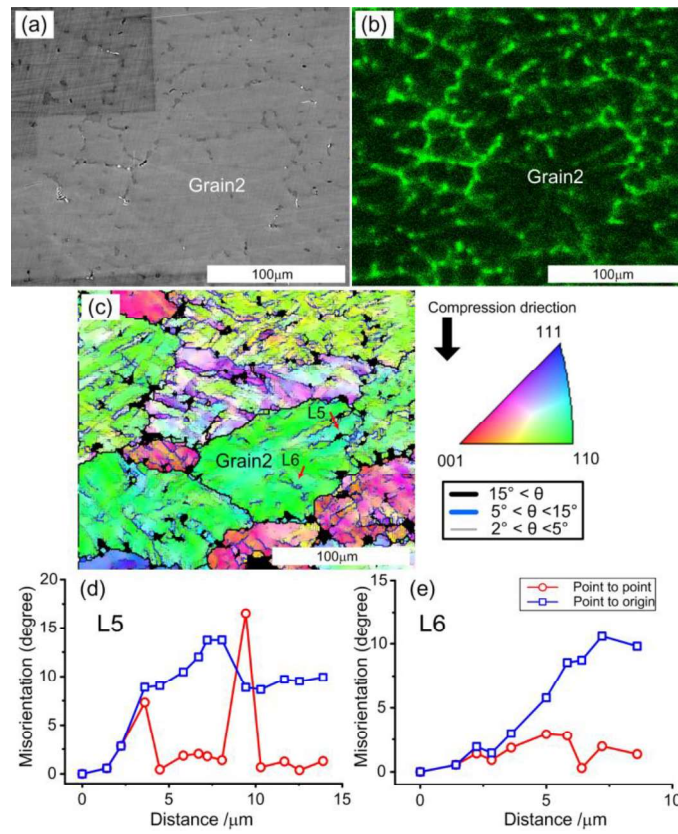


Figure 3 (a)-(c) SEM, EDS and EBSD maps for the sample with $\epsilon = 0.45$ at RT, respectively; and (d) and (e) misorientation profiles measured along L5 and L6 in Fig. 3(c), respectively. The unit triangle denotes the crystallographic orientations.

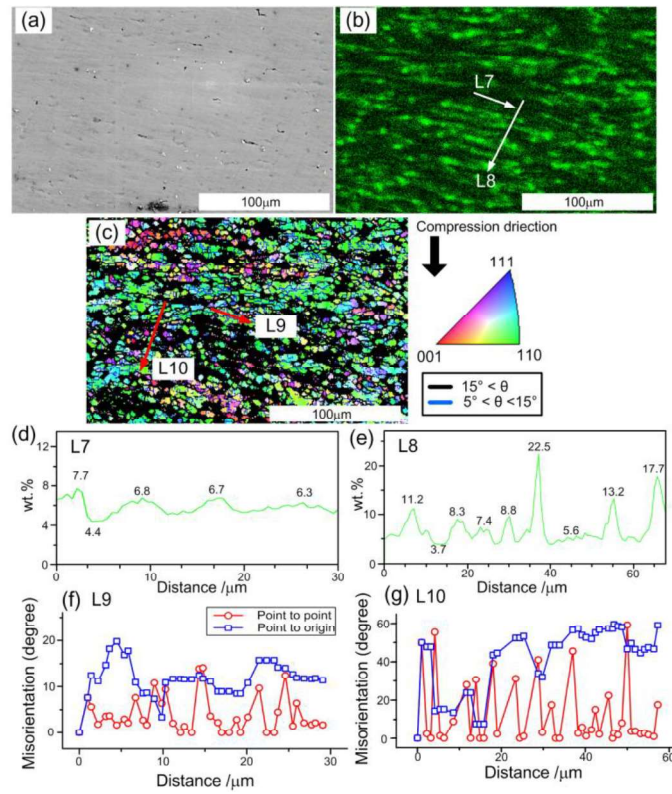


Figure 4 (a)-(c) SEM, EDS and EBSD maps for the sample with $\epsilon = 0.97$ at RT, respectively; (d) and (e) EDS line profiles of Mg concentration along L7 and L8 in Fig. 4(b); and (f) and (g) misorientation profiles measured along L9 and L10 in Fig. 4(c).

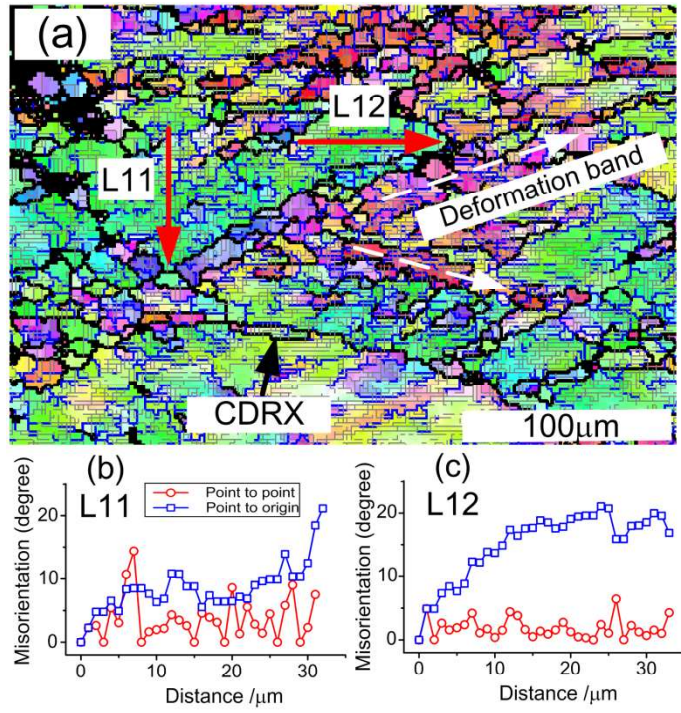


Figure 5 (a) Typical EBSD map for the sample with $\epsilon = 0.97$ at RT; and (b) and (c) misorientation profiles measured along L11 and L12 in Fig. 5(a), respectively.

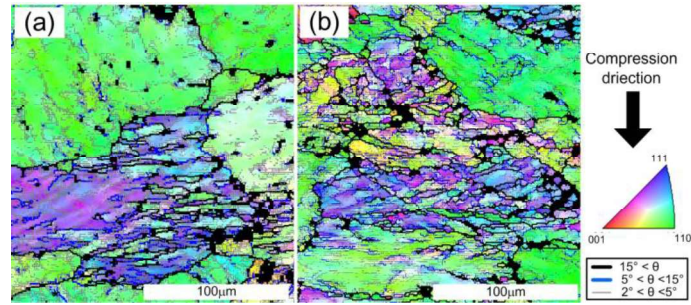


Figure 6 Typical EBSD maps of the TD-RD plane of Al-7Mg samples after deformed to different strains:

(a) $\epsilon = 0.25$ and (b) $\epsilon = 0.43$ at LNT.

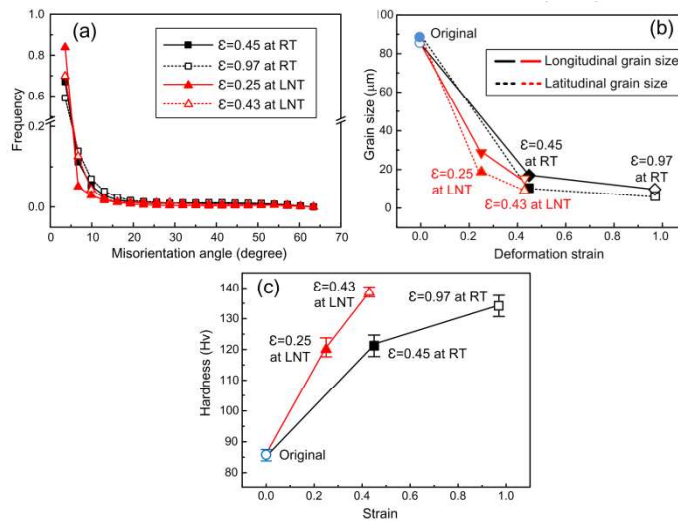


Figure 7 (a) Misorientation distribution with increasing strain at RT and LNT; and (b) grain sizes and (c) hardness of the DPD samples with different strains.